Steel and Composite Structures, *Vol. 36, No. 6 (2020) 703-710*
DOI: https://doi.org/10.12989/scs.2020.36.6.703

Strain rate effect of steel-concrete composite panel indented by a hemispherical rigid body

Weiyi Zhao[1a], Lin Wang[*2], Guotao Yang[1b], Ziguo Wang[1c], Zepeng Gao[1d] and Quanquan Guo[3e]

[1]Department of Civil Engineering, Qingdao University of Technology, Qingdao 266033, Shandong, China
[2]Beihang School, Beihang University, Beijing 100191, China
[3]School of Transportation Science and Engineering, Beihang University, Beijing 100191, China

(*Received December 12, 2019, Revised September 9, 2020, Accepted September 11, 2020*)

Abstract. This paper presents numerical and theoretical investigations on the strain rate in steel-concrete composite (SC) panels under low-velocity impact of a hemispherical rigid body. Finite element analyses were performed on five specimens with different loading rates. The impact energy was kept constant to eliminate its influence by simultaneously altering the velocity and mass of the projectile. Results show that the strain rate in most parts of the specimens was low and its influence on bearing capacity and energy dissipation was limited in an average sense of space and time. Therefore, the strain rate effect can be ignored for the analyses of global deformation. However, the strain rate effect should be considered in local contact problems. Equations of the local strain and strain rate were theoretically derived.

Keywords: steel-concrete composite panel; finite element analysis; low-velocity impact; strain rate; theoretical method

1. Introduction

A steel-concrete composite (SC) panel typically consists of two steel plates connected to a plain concrete core by means of mechanical shear connectors. The SC panels have been widely used in nuclear facilities, high-rise buildings, offshore platforms, and protective structures (Varma *et al.* 2014, Hilo *et al*. 2015). Since these structures are exposed under unexpected impact loadings during their service life, the evaluation of the dynamic response of the structural elements is one of the primary concerns (Cox *et al.* 2006, Jiang and Chorzepa 2014, Sadiq *et al*. 2014).

In engineering practice, the quasi-static analysis is a common approach for the design of structures subjected to impact loadings (Jones 1989, Abrate 1998, Davies and Olsson 2004). It is assumed in the analysis that the resistance function of the structure subjected to the same spatial distribution of load, but applied statically can be used. Thus, the theoretical and numerical analyses are simplified effectively with acceptable accuracy. It is noted that a precondition for using this method is that the failure mode of the structure under impact is the same as that under static load.

Unfortunately, concrete is a kind of brittle material. Investigations show that the failure mode of reinforced concrete (RC) components may change with the increase of the loading rate (Ožbolt and Sharma 2011; Micallef et al. 2014). Besides, concrete and mild steel are strain rate sensitive materials so that the influence of the strain rate should be adequately assessed (ACI 349-01 2006; ANSI/AISC N690s1-15 2015).

To date, several studies were carried out on the dynamic response of SC panels subjected to low-velocity impact. Remennikov *et al.* (2012, 2013) carried out drop hammer impact test on axially restrained SC panels. Sohel and Liew (2014) performed drop hammer impact tests on SC panels with J-hook connectors and proposed an energy balanced model for evaluating the maximum deformation. Bruhl *et al.* (2015) conducted numerical investigations and developed equations for the static resistance function, which can be used in single-degree-of-freedom (SDOF) analyses of SC panels. Guo and Zhao (2019) derived a theoretical resistance function model for SDOF analyses and proposed a design method for SC panel under low-velocity impact.

It is noted that the strain rate effect was ignored in the previous investigations of SC panels. But its influence on the calculated results was not quantitatively evaluated and was still unknown. In this paper, numerical analyses are performed on four SC panel specimens under impact and one under quasi-static loading. The velocity and mass of the projectiles are altered simultaneously to retain a constant impact energy in each analysis. According to the results of the strain rate distributions in the specimens under different loading rates, the influence of the strain rate on the global deformation and local deformation is discussed. A theoretical method for evaluating the local stretching strain and strain rate is further developed and provides a reference for the analyses of local contact problems.

*Corresponding author, Ph.D., Lecturer
E-mail: wlccdq@163.com
[a]Associate professor
[b]Professor
[c]Ph.D.
[d]Graduate student
[e]Professor

ISSN: 1229-9367 (Print), 1598-6233 (Online)

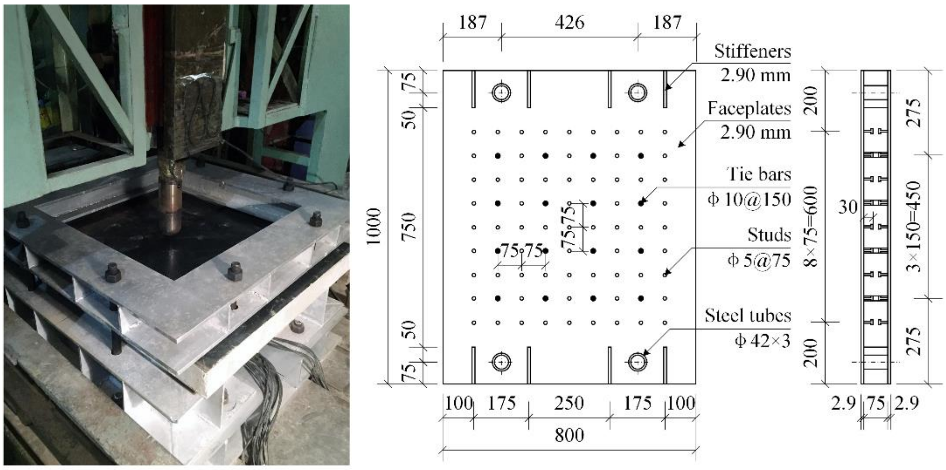

(a) Test set-up (b) Drawing of the specimen

Fig. 1 Test set-up and typical drawing of the SC panel specimens

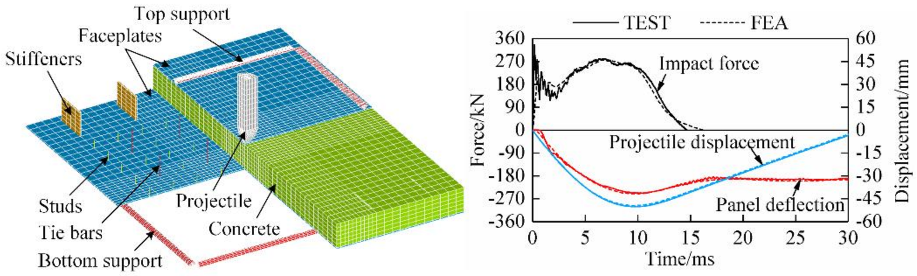

(a) Cutaway view of the FE model (b) Predicted and experimental impact histories

Fig. 2 FE model and dynamic response results

2. Numerical investigations

2.1 Finite element models

Previously, Zhao *et al*. (2018) conducted drop hammer impact tests on SC panel specimens. Fig. 1 shows the impact test set-up and a typical drawing of the specimens. To predict the impact response of the SC panels, three-dimensional finite element (FE) models were developed using LS-DYNA Version 971 (Hallquist 2010). Fig. 2 gives a cutaway view of the FE model and the predicted and experimental impact histories of Specimen H45. The comparison of the failure modes and impact histories between the test results and the calculated results in literature has shown the efficiency and accuracy of the proposed models. In this paper, numerical investigations on the strain rate effect of the SC panels under low-velocity impact were carried out based on the test specimens and the validated FE models.

As shown in Fig. 1(b), the dimensions of all specimens were 1000 mm×800 mm (length × width). The thicknesses of the steel plates and the core concrete were 2.90 mm and 75 mm, respectively. The studs with diameter of 5 mm were arranged on the inner surface of the steel plates at a spacing of 75 mm. The diameter and the spacing of the tie bars were 10 mm and 150 mm, respectively.

As shown in Fig. 2(a), for the concrete, support rollers, and the projectile, solid elements (Solid164) were used. The steel plates were modeled using Belytschko-Tsay shell elements (Shell163). The Hughes-Liu with cross section integration beam elements (Beam161) were used to model the studs and the tie bars. From a convergence study, the mesh size was determined to be 12.5 mm near the impact point and a coarse size of 25 mm was used for other regions to save computation time without loss of accuracy (Zhao *et al.* 2018). The coincident nodes of the steel plates and the studs/tie bars were merged in the FE models to simulate a perfect weld condition and likewise for the coincident nodes of the concrete and the connectors assuming full bond was achieved.

For the steel plates and the connectors, the Plastic Kinematic material model (*MAT_003) was used. With the constitutive equation proposed by Cowper and Symonds (1957), the strain rate effect of mild steel was considered. As shown in Eq. (1), σ_d is the dynamic stress at a uniaxial strain rate ε, σ_s is the associated static stress, and C and q are coefficients.

$$\frac{\sigma_{\mathrm{d}}}{\sigma_{\mathrm{s}}}=1+\left(\frac{\dot{\varepsilon}}{D}\right)^{1/q} \tag{1}$$

The CSCM concrete model (*MAT_159) was applied to the infilled concrete. This material model was frequently used in recent studies and found to be effective in predicting the performance of structures subjected to low-velocity impact loadings. The parameters can be generated automatically by providing basic material properties such as unconfined compressive strength, density, and aggregate size. The strain rate effect model is turned on by setting IRATE=1.

For the supports and the projectile, the rigid material model (*MAT_020) was used assuming that they are elastic during impact. The projectiles with different masses shared the same geometric model for simplicity. Through altering the density, the mass of the projectile can be set to any required values.

The input values for the material models are summarized in Table 1.

The translational degree-of-freedom of the nodes of the supports were restrained. The projectile was released using *INITIAL_VELOCITY_GENERATION keyword at the designed initial velocity. The interactions between different parts in the model were defined by Automatic-Surface-to-Surface contact algorithm. The contact pairs include: (1) the supports and the steel plates; (2) the concrete and the steel plates; (3) the projectile with the steel plates and the concrete. The static and dynamic coefficients of friction applied to the interfaces between the concrete and the steel plates were 0.3 and 0.1, respectively. The friction between the projectile and the specimen was ignored. In addition, the hourglass energy was controlled using Flanagan-Belytschko with exact volume integration (type 3). A default value of 0.1 was used for the hourglass coefficient.

2.2 Loading conditions

The strain rate of the SC specimen under impact depends on the loading rate, i.e. the impact velocity of the projectile.

Table 1 Material properties for the FE models

Material model	Variable		Unit	Value
*MAT_003 (steel plates and connectors)	Mass density	RO	ton·mm^{-3}	7.8×10^{-9}
	Young's modulus	E	N·mm^{-2}	2.1×10^{5}
	Poisson's ratio	PR		0.3
	Tangent modulus	ETAN	N·mm^{-2}	6.3×10^{3}
	Yield stress	SIGY	N·mm^{-2}	287
	Failure strain	FS		0.3
	Strain rate parameter	SRC		40.5
	Strain rate parameter	SRP		5
*MAT_159 (concrete)	Mass density	RO	ton·mm^{-3}	2.3×10^{-9}
	Compressive strength	FPC	N·mm^{-2}	48.7
	Maximum aggregate size	DAGG	mm	10
*MAT_020 (projectile and supports)	Mass density	RO	ton·mm^{-3}	7.8×10^{-9}
	Young's modulus	E	N·mm^{-2}	2.1×10^{5}
	Poisson's ratio	PR		0.3

Table 2 Loading conditions

Specimen	m /kg	v_0 /m·s^{-1}	mv_0 /kg·m·s^{-1}	E_0 /kJ
V04	1093.8	4	4375.0	8.75
V08	273.4	8	2187.5	8.75
V16	68.4	16	1093.8	8.75
V32	17.1	32	546.9	8.75

However, the impact velocity is not an independent variable because its value determines the impact energy (kinetic energy of the projectile). During impact, the impact energy is transformed into the elastic and plastic deformation energies of the SC panel. Therefore, the response of the SC panel is directly affected by the impact energy.

To consider different strain rates and exclude the influence of the impact energy, the mass and the impact velocity were both altered at the same time to retain a fixed impact energy in the analyses. As shown in Table 2, four specimens under impact were analyzed using the FE models, where the letter "V" and the following number denote the impact velocity. According to the experiment carried out by Zhao *et al.* (2018), an impact energy of 8.75 kJ was selected for all specimens. The specimens were expected to develop plastic deformations but without failure. Table 2 lists the mass (m), velocity (v_0), momentum (mv_0), and energy (E_0) of the projectiles.

One control specimen (V00) under quasi-static loading was also analyzed. Displacement loading was applied through the projectile with a constant speed of 0.1 m·s^{-1}. The corresponding maximum strain rate in the specimen was about 0.01-0.1 s^{-1} during loading, which was within the range for a quasi-static loading.

3. Results and discussions

3.1 Load-displacement relations

Fig. 3 shows the load-displacement relations of all five specimens. Here, the load refers to the contact force between the projectile and the specimen, and the displacement refers to the displacement of the projectile. For Specimen V00, the load-displacement relation was almost linear before yielding. Subsequently, with the increase of the displacement, membrane stresses developed in the specimen and the load continued to increase. The load-displacement relation is different from those of simply supported beams, because the membrane effect always exists in large deformed plates with non-zero Gaussian curvature, even if no boundary restrains are provided (Jones 1989, Yu and Chen 1990).

With the increase of the impact velocity, the inertial effect started to appear gradually. Fig. 3 shows that the loading curves of the specimens V04 and V08 coincided with that subjected to quasi-static loading. However, there were "inertial peaks" in the load-displacement relations of

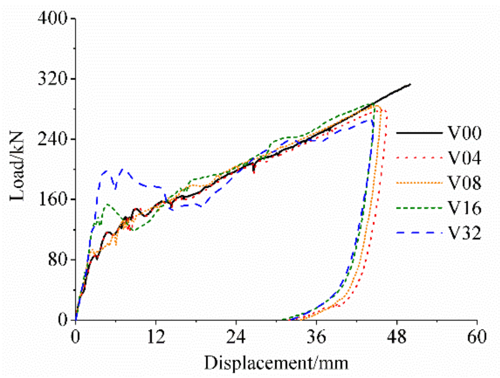

Fig. 3 Load-displacement relations

Table 3 Analysis results

Specimen	W_p /kJ	y_{max} /mm	w_{max} /mm	P_{max} /kN	&&max /s^{-1}
V04	7.99	46.6	38.2	8.8	8.2
V08	8.00	45.6	37.1	18.0	13.8
V16	7.96	44.7	36.6	36.4	24.1
V32	7.94	44.5	36.7	65.2	42.2

V16 and V32. When the projectile and the specimen first came into contact, the particles of the specimen were forced to accelerate to the speed of the projectile. The inertial force, according to D'Alembert principle, was responsible for the sharp change in the impact force. As shown in Fig. 3, the higher the impact velocity the greater the peak value.

Except for the inertial response, the load-displacement relations of all specimens were almost the same. Moreover, the loading and unloading stiffnesses of the specimens under impact were also the same with the loading stiffness of the specimen under quasi-static loading.

The plastic work done on the specimen (W_p) can be calculated by integrating the area under the load-displacement curve, which also represents the energy absorbed by the plastic deformation of the specimen and dissipated by the structural damping. Table 3 shows that the values of W_p were about 8 kJ for all specimens, accounting for 90% of the impact energy. The other 10% of the impact energy first transformed to the elastic deformation energy of the specimen, then again to the kinetic energy of the projectile. Table 3 also gives the maximum displacement of the projectile (y_{max}) and the maximum deflection of the specimen (w_{max}). It shows that the deformations slightly decreased with the increase of the impact velocity.

3.2 Influence of the inertial force

Banthia (1987) proposed a method for separating the inertial force from the impact force. By measuring the acceleration of the specimen at the center and assuming the acceleration distribution based on first mode vibration, the inertial force can be evaluated using the virtual work principle. However, the method is not accurate because the influence of the higher mode vibrations cannot be considered (Fujikake *et al.* 2009).

Hrynyk and Vecchio (2014) measured the accelerations of steel fiber-reinforced concrete slab specimens at eight locations in the impact tests. It was found that the acceleration distribution varied with time and showed no regularity due to the higher mode vibrations. The inertial force was computed by integrating the acceleration distribution and exhibited reasonable accuracy.

With the FE results in this paper, the acceleration and displacement distributions at any time step are easy to access. As shown in Fig. 4, the inertial force $P(t)$ can be computed based on the virtual work principle. A discrete form formula is given as

$$P(t) = \frac{\sum_i m_i \ddot{u}_i(t) \delta t_i(t)}{\delta u_0(t)} \tag{2}$$

where, m_i is the mass of the elements in a certain range around Node i, $\ddot{u}$ (t) is the vertical acceleration of Node i at time t, $\delta u_i(t)$ is the virtual vertical displacement of Node i at time t, and $\delta u_0(t)$ is the virtual vertical displacement of the central node at time t.

It was assumed that the specimen responses were reasonably symmetric, and the changes of acceleration and displacement along the thickness direction were ignored. Thus, the mid-plane nodes of one quarter of the specimen were taken for the calculation. The real displacements of the nodes were used instead of virtual displacements.

Fig. 5 presents the inertial force and impact force time histories. It clearly shows that the inertial effect increased with the increase of the impact velocity. As given in Table 3, the maximum inertial forces (P_{max}) of the four specimens under impact were 8.8 kN, 18.0 kN, 36.4 kN, and 65.2 kN, respectively. A linear relation between the inertial force and the impact velocity can be observed.

Taking Specimen V32 as an example, the inertial force accounted for 40% of the impact force at the first peak (inertial peak). Then the inertial force rapidly reduced to less than 10% of the impact force. It demonstrates that the inertial effect had a great influence on the response within the first 1 ms.

By integrating the area under the inertial force-displacement curve, it is found that the work done by the inertial force was close to zero (less than 0.1 kJ). Therefore, the influence of the inertial force on the energy dissipation can be excluded.

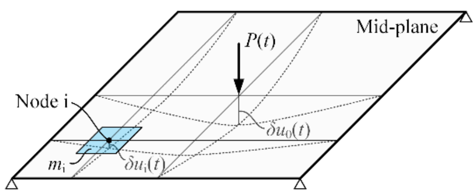

Fig. 4 Evaluation of the inertial force

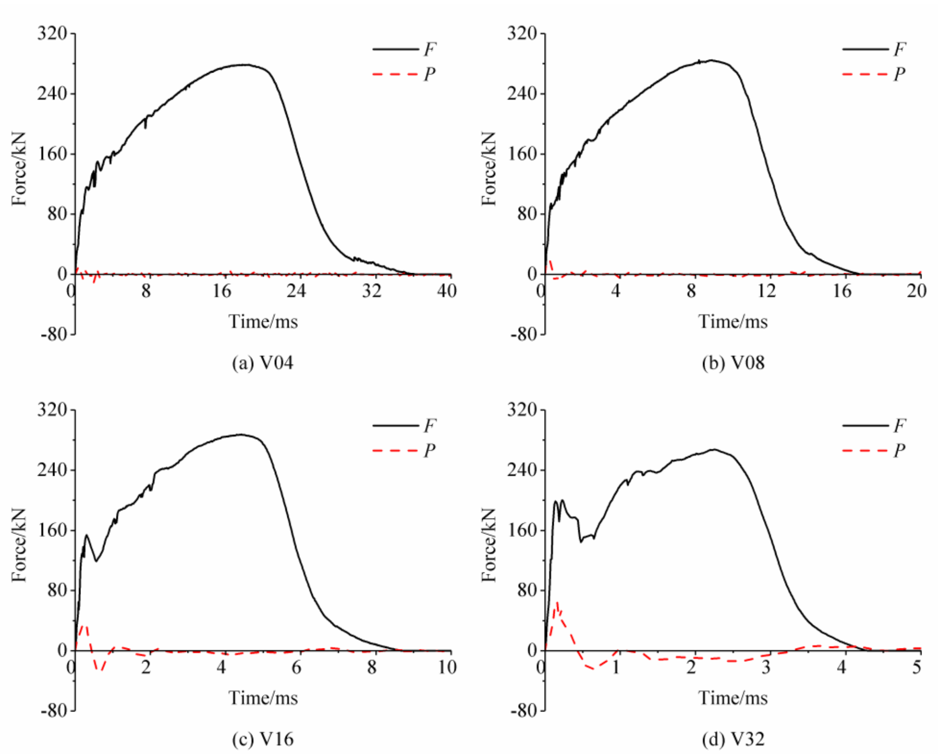

Fig. 5 Inertial force and impact force time histories

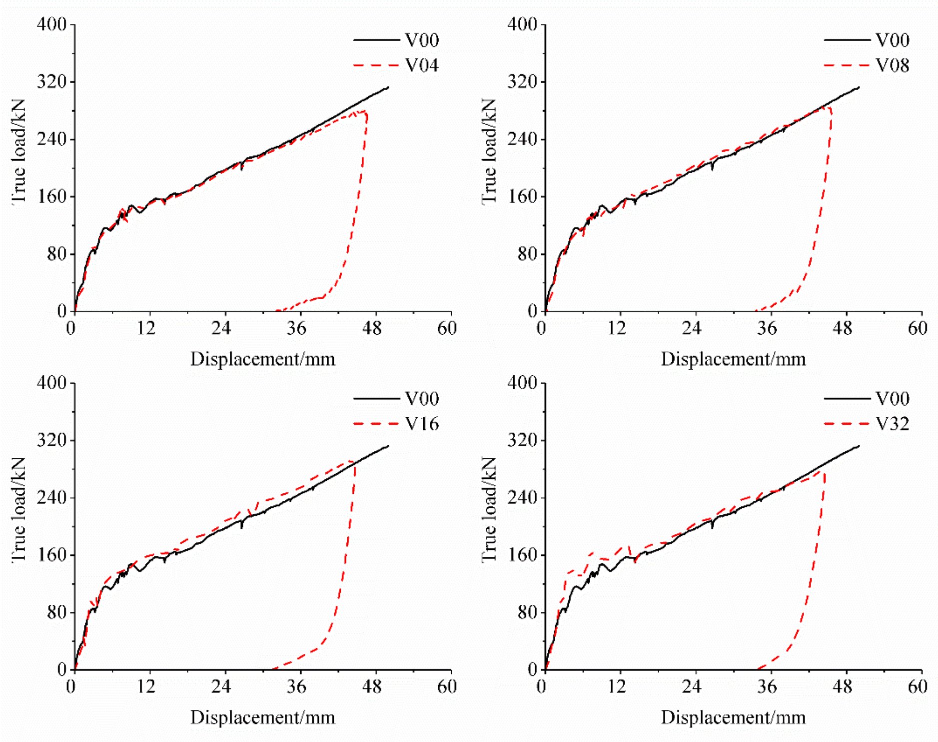

Fig. 6 True load-displacement relation

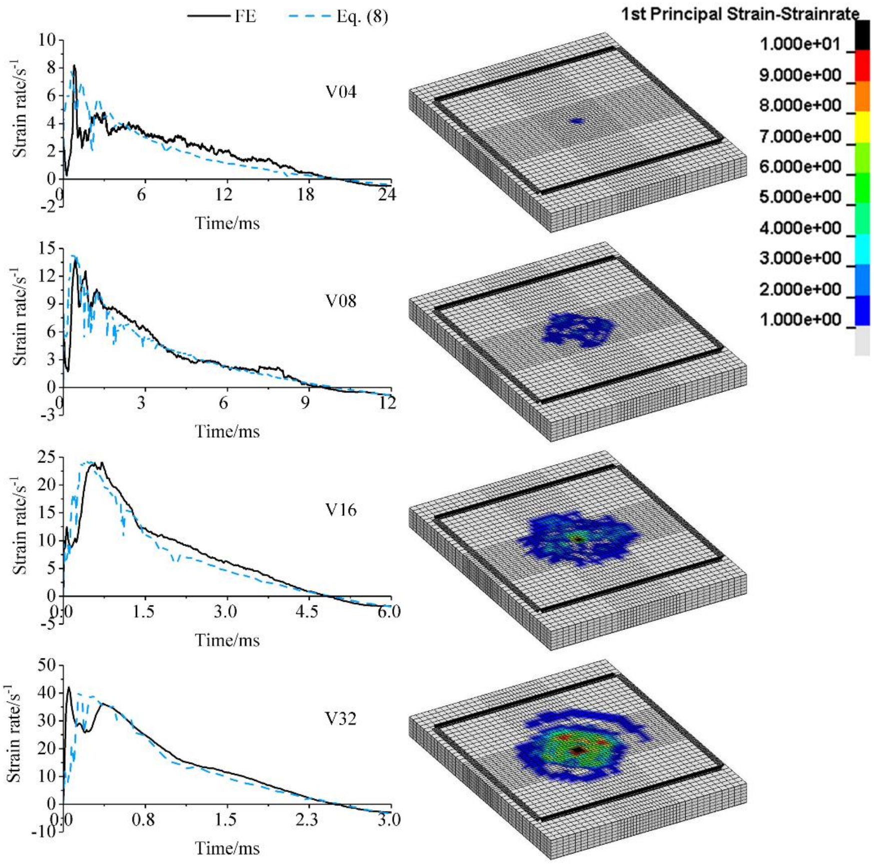

Fig. 7 Strain rate distributions

3.3 Strain rate effect

The "true load" applied on the specimen can be calculated by subtracting the inertial force from the impact force. Fig. 6 shows that the true load-displacement relations of Specimens V04 and V08 agreed well with the load-displacement relation of Specimen V00; while for Specimens V16 and V32, the true load increased by up to 12% and 21% around yielding, respectively. From Fig. 6 and Table 3, it can be observed that the bearing capacity and energy dissipation capacity of the specimen were slightly enhanced under impact due to the strain rate effect.

To further study the influence of the strain rate effect, the 1st-principle-strain strain rate distributions of the specimens at maximum values are plotted in Fig. 7. The FE results show that the strain rate in the gray area was less than 1 s^{-1} and fell within the range for a quasi-static loading. In the very local region near the impact position (black area), the strain rate was much larger and exceeded 10 s^{-1}.

Fig. 7 also gives the strain rate-time history of the element at the impact position. It shows that the strain rate varied over time. As the projectile came into contact with the specimen, the strain rate increased sharply to a peak value. Table 3 summarizes the values of the maximum strain rate around the impact position $\dot{\varepsilon}_{\max}$. While the kinetic energy of the projectile transformed to the deformation energy of the specimen, the motion velocity slowed down and the strain rate decreased. The instantaneous strain rate was zero when the specimen reached the maximum deformation. Then it turned to a negative value because the elastic energy stored in the specimen began to release.

Previous studies showed that the yield capacity of the SC specimens can be evaluated by the yield line mechanism (Yan and Liew 2016). As the thicknesses of the steel plates on both sides are the same, the yield capacity is linearly related to the yield strength of the steel plate. For mild steel used in this study, a strain rate of 10 s^{-1} indicates that the dynamic increasing factor (DIF) of the yield strength is 1.76. It is noted that the strain rate in most part of the specimen is small. Therefore, it is reasonable that the bearing capacity only increased by 10-20% in an average sense. Moreover, since the strain rate decreased over time, the enhancements in the bearing capacity and energy dissipation capacity were limited. Consequently, the maximum deflection only decreased by up to 4% (from 38.2 mm to 36.6 mm, as shown in Table 3).

In structural design, the displacement response could be underestimated if the strain rate effect is considered, which is unsafe for the equipment to be protected in the structure. Therefore, it is suggested that the strain rate effect can be ignored in the global displacement analysis of SC panels under low-velocity impact.

4. Theoretical method for evaluating the local strain and strain rate

Actually, the quasi-static load-displacement relation is commonly used in the single-degree-of-freedom method or energy method to evaluate the displacement response for simplicity (Sohel and Liew 2014, Bruhl *et al.* 2015, Guo and Zhao 2019). The above discussion shows that this simplification is effective with acceptable accuracy. However, for the local region under impact, the strain rate effect is large and cannot be ignored. In this paper, a theoretical method for calculating the strain rate of SC panels struck by a spherical object is provided. It can be used in the analyses of the local regions.

As shown in Fig. 8, Sohel and Liew (2014) derived an equation of the elastic strain energy for local indentation of the steel plate. Based on the principle of minimum potential energy, the relation between the indentation depth δ, the indentation radius a, and the contact force F is given as

$$F = \frac{1.282\pi t_s E_s \delta^3}{a^2} + \frac{\pi a^2 \delta E_c}{5t_c} \tag{3}$$

where, t_s and t_c are the thicknesses of the steel plates and core concrete, respectively; and E_s and E_c are the Young's moduli of the steel plates and core concrete, respectively.

Then, $\partial F/\partial a$=0 gives

$$a^2 = \left(\frac{6.41 t_s t_c E_s}{E_c}\right)^{0.5} \delta \tag{4}$$

As shown in Fig. 9, a linear relation between a^2 and δ can be observed in the experimental data obtained in the previous research by Zhao *et al.* (2018). The varied parameters include the thickness and strength of the steel plates and the impact energy. It is noted that Eq. (4) depicts the linear relation well, but without enough accuracy. Considering the development of plasticity in the impact events, Eq. (4) is modified as follow

$$a^2 = \left(\frac{6.41 t_s t_c E_s}{E_c}\right)^{0.5} \delta \tag{5}$$

where, f_y is the yield strength of the steel plate, and f_c is the compressive strength of the core concrete.

Fig. 9 shows that the values calculated by Eq. (5) agree well with the experimental results after introducing the strength parameters of the steel plates and core concrete.

Meanwhile, the strain in the radial direction at the impact position can be estimated as (Sohel and Liew 2014)

$$\varepsilon \approx 0.5\left(\frac{\delta}{a}\right)^{0.5} \tag{6}$$

Substituting Eq. (5) into Eq. (6) gives

$$\varepsilon \approx 1.26\delta^{0.25}\left(E_c f_c / t_s t_c E_s f_y\right)^{0.125} \tag{7}$$

Taking the derivative of the strain with respect to time, the strain rate is obtained

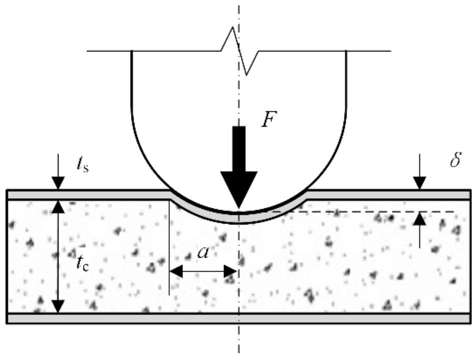

Fig. 8 Local indentation of SC panels

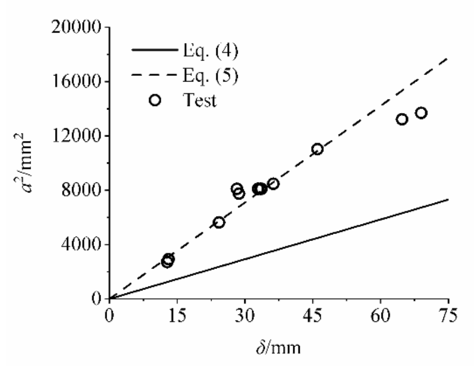

Fig. 9 Comparison between Eqs. (4) and (5)

$$\dot{\varepsilon} \approx 0.315\delta^{-0.75}(E_c f_c / t_s t_c E_s f_y)^{0.125}\dot{\delta} \tag{8}$$

For a dynamic analysis solved by finite difference method, the indentation depth obtained in Step n can be used to calculate the strain rate by Eq. (8). Then the load-displacement relation in Step n+1 can be modified based on the strain rate. In this study, such an analysis is beyond the scope of discussion. Instead, the strain rate time histories of the specimens are calculated using the indentation depth measured from the FE results. Fig. 7 presents the comparison between the calculated strain rate time histories and the FE results. It shows that both the peak values and durations are in good agreement.

5. Conclusions

The strain rate effect in SC panels subjected to low-velocity impact was numerically and theoretically studied. In the FE results, the strain rate distribution in most parts of the specimen was low and the influence on the bearing capacity and energy dissipation capacity was not obvious. It is suggested that the strain rate effect can be ignored in the dynamic analysis of the global deformation of SC panels under low-velocity impact.

A theoretical method for evaluating the stretching strain and strain rate in the local region was developed. The calculated results were compared with existing test results and FE results to verify its accuracy. The proposed equations provide a tool for solving local contact problems.

Further work is in progress to develop a two-degree-of-freedom model considering the local contact.

Acknowledgments

This work was supported by National Natural Science Foundation of China [grant numbers 52008219 and 51808308]. The supports are gratefully acknowledged.

References

Abrate, S. (1998), *Impact on Composite Structures*, Cambridge University Press, USA.

ACI 349-01 (2006), *Code Requirements for Nuclear Safety-Related Concrete Structures and Commentary*, American Concrete Institute; Farmington Hills, MI, USA.

ANSI/AISC N690s1-15 (2015), *Specification for Safety-Related Steel Structures for Nuclear Facilities*, American Institute of Steel Construction; Chicago, Illinois, USA.

Banthia, N.P. (1987), "Impact resistance of concrete", Ph.D. Dissertation; University of British Columbia, Canada.

Bruhl, J.C., Varma, A.H. and Kim, J.M. (2015), "Static resistance function for steel-plate composite (SC) walls subject to impactive loading", *Nucl. Eng. Des.*, **295**, 843-859. https://doi.org/10.1016/j.nucengdes.2015.07.037.

Davies, G.A.O. and Olsson, R. (2004), "Impact on Composite Structures", *Aeronautical J.*, **108**, (1089), 541-563. https://doi.org/10.1017/S0001924000000385.

Fujikake, K., Li, B. and Soeun, S. (2009), "Impact response of reinforced concrete beam and its analytical evaluation", *J. Struct. Eng.*, **135**(8), 938-950. https://doi.org/10.1061/(ASCE)ST.1943-541X.0000039.

Guo, Q. and Zhao, W.Y. (2019), "Design of steel-concrete composite walls subjected to low-velocity impact", *J. Constr. Steel Res.*, **154**, 190-196. https://doi.org/10.1016/j.jcsr.2018.12.001.

Hallquist, J.O. (2010), *LS-DYNA keyword user's manual, vol. 1, Version 971*, Livermore Software Technology Corporation (LSTC)

Hilo, S.J., Badaruzzaman, W.H.W., Osman, S.A., Al-Zand, A.W., Samir, M. and Hasan, Q.A. (2015), "A state-of-the-art review on double-skinned composite wall systems", *Thin-Wall. Struct.*, **97**, 74-100. https://doi.org/10.1016/j.tws.2015.09.007.

Hrynyk, T.D. and Vecchio, F.J. (2014), "Behavior of steel fiber-reinforced concrete slabs under impact load", *ACI Struct. J.*, **111**(5), 1213-1224. https://doi.org/10.14359/51686923.

Jiang, H. and Chorzepa, M.G. (2014), "Aircraft impact analysis of nuclear safety-related concrete structures: A review", *Eng. Failure Anal.*, **46**, 118-133. https://doi.org/10.1016/j.engfailanal.2014.08.008.

Jones, N. (1989), *Structural Impact*, Cambridge University Press, UK.

Micallef, K., Sagaseta, J., Ruiz, M.F. and Muttoni, A. (2014), "Assessing punching shear failure in reinforced concrete flat slabs subjected to localised impact loading", *Int. J. Impact Eng.*, **71**(6), 17-33. https://doi.org/10.1016/j.ijimpeng.2014.04.003.

Ožbolt, J. and Sharma, A. (2011), "Numerical simulation of reinforced concrete beams with different shear reinforcements under dynamic impact loads", *Int. J. Impact Eng.*, **38**(12), 940-950. https://doi.org/10.1016/j.ijimpeng.2011.08.003.

Remennikov, A.M. and Kong, S.Y. (2012), "Numerical simulation and validation of impact response of axially-restrained steel–concrete–steel sandwich panels", *Compos. Struct.*, **94**(12), 3546-3555. https://doi.org/10.1016/j.compstruct.2012.05.011.

Remennikov, A.M., Kong, S.Y. and Uy, B. (2013), "The response of axially restrained non-composite steel–concrete–steel sandwich panels due to large impact loading", *Eng. Struct.*, **49**, 806-818. http://dx.doi.org/10.1016/j.engstruct.2012.11.014.

Sadiq, M., Xiuyun, Z. and Rong, P. (2014), "Simulation analysis of impact tests of steel plate reinforced concrete and reinforced concrete slabs against aircraft impact and its validation with experimental results", *Nucl. Eng. Des.*, **273**, 653-667. https://doi.org/10.1016/j.nucengdes.2014.03.031.

Sohel, K.M.A. and Liew, J.Y.R. (2014), "Behavior of steel–concrete–steel sandwich slabs subject to impact load", *J. Constr. Steel Res.*, **100**, 163-175. https://doi.org/10.1016/j.jcsr.2014.04.018.

Varma, A.H., Malushte, S.R., Sener, K.C. and Lai, Z. (2014), "Steel-plate composite (SC) walls for safety related nuclear facilities: Design for in-plane forces and out-of-plane moments", *Nucl. Eng. Des.*, **269**, 240-249. https://doi.org/10.1016/j.nucengdes.2013.09.019.

Yan, J.B. and Liew, J.Y.R. (2016), "Design and behavior of steel–concrete–steel sandwich plates subject to concentrated loads", *Compos. Struct.*, **150**, 139-152. https://doi.org/10.1016/j.compstruct.2016.05.004.

Yu, T. and Chen, F. (1990), "Analysis of the large deflection dynamic plastic response of simply-supported circular plates by the "membrane factor method", *Acta Mechanica Sinica*. **6** (4), 333-342. https://doi.org/10.6052/0459-1879-1990-5-1995-984.

Zhao, W., Guo, Q., Dou, X., Zhou, Y. and Ye, Y. (2018), "Impact response of steel-concrete composite panels: Experiments and FE analyses", *Steel Compos. Struct.*, **26**(3), 255-263. https://doi.org/10.12989/scs.2018.26.3.255.

BU